Progress In Electromagnetics Research B, Vol. 101, 101–117, 2023

A Uniform Additional Term Using Fock-Type Integral to Unify Edge Diffraction, Creeping Diffraction, and Reflection in Lit and Shadowed Regions

Xin Du* **and Jun-Ichi Takada**

Abstract—The uniform geometrical theory of diffraction (UTD) calculating edge diffraction, creeping diffraction, and reflection has been widely used to predict the shadowing problems for the beyond 5th generation. The limitation of the previous work, which only discussed the relationship between edge diffraction and reflection in the lit region, has motivated the analysis of the difference between creeping diffraction and edge diffraction in the shadowed region. In this paper, as the difference between creeping diffraction and edge diffraction from a dielectric circular cylinder and an absorber screen, respectively, a novel additional term is derived based on the UTD in the shadowed region. In addition, a uniform additional term using the Fock-type integral is proposed to unify the formulations in the lit and shadowed regions. The proposed uniform additional term is validated by the UTD and exact solutions of a dielectric circular cylinder at millimeter-wave or sub-terahertz bands. From the discussion of the results, the proposal can not only unify the formulations in the lit and shadowed regions but also eliminate the fictitious interference. Through the proposal, we can separate the contribution of the shadowed Fresnel zone number (FZ) and boundary conditions (i.e., the surface impedance and polarization). The frequency characteristics of the shadowed FZ and boundary conditions are analyzed and simulated near a shadow boundary at a high frequency (10 GHz–100 GHz). The results imply that there is almost no dependency (less than 1 dB) on boundary conditions in the lit region while there are a few dependencies (more than 1 dB) on boundary conditions in the shadowed region. This work attempts to unify three different propagation mechanisms, i.e., reflection, edge diffraction, and creeping diffraction, by using one formula.

1. INTRODUCTION

The uniform geometrical theory of diffraction (UTD) [1–5] has been widely used to predict the performance of antennas, radar cross sections [6–8], and human-body shadowing problem at millimeter-wave (mmWave) or sub-terahertz (sub-THz) band in the beyond 5th generation (B5G) mobile communication systems [9–14]. The UTD based on Fermat's principle provides the closed-form analytic solutions of edge diffraction, creeping diffraction, and reflection [1–5]. The coefficients of reflection and diffraction are derived from the exact solutions of the canonical problems [15]. In the exact solutions, the total field can be represented as the sum of the infinite series of the Hankel and Bessel functions [15]. The UTD approximates the Hankel function as the first term of its asymptotic expansion in high frequency and replaces the Bessel function with contour integrals in the complex plane. Through the Pauli-Clemmow modified method of steepest descent [16] and residue evaluation in the complex plane [17], the total fields can be calculated by the uniform coefficients, which overcome the disadvantage of a

Received 17 April 2023, Accepted 21 June 2023, Scheduled 15 July 2023
* Corresponding author: Xin Du (du.x.ab@m.titech.ac.jp).
The authors are with the Department of Transdisciplinary Science and Engineering, School of Environment and Society, Tokyo Institute of Technology, Japan.

discontinuity at the shadowing boundary in the geometrical theory of diffraction (GTD) [18]. Compared with the numerical methods such as the Kirchhoff approximation (KA) [19–22] and the physical theory of diffraction (PTD) [23, 24], the UTD using analytic uniform coefficients can achieve a faster prediction with a lower computational load at a high frequency.

In a 2-dimensional problem, there are mainly two kinds of canonical problems, i.e., the wedge and circular cylinder. Therefore, two types of UTD calculations exist. One of them calculates edge diffraction from a wedge [1, 2], and the other calculates creeping diffraction and reflection from a circular cylinder [3–5]. Similarly, there are mainly two types of modeling for the human body in shadowing problems. One of them models the human body as an absorber screen [15, 25, 26], which can be seen as the wedge with a wedge angle of zero. The other models the human body as a dielectric circular cylinder [27–31], which considers the permittivity of the human skin.

In our previous work [32], a formula to unify edge diffraction and reflection from the absorber screen and circular cylinder, respectively, was proposed in the lit region. Through [32], a reflected field from a dielectric circular cylinder can be separated as an edge diffraction from an absorber screen and an additional term. The work in [32] also showed a detailed derivation of that the diffraction from an absorber screen is determined by the shadowed Fresnel zone (FZ) alone while the additional term is determined by the boundary conditions (i.e., surface impedance and polarization) only. In addition, the work in [32] analyzed that the edge diffracted field separated from the reflected field becomes dominant near a shadow boundary (SB) when the frequency increases. Therefore, the work in [32] figured out that the contribution of the FZ is larger than the contribution of the boundary conditions in the lit region near the SB, especially at a high frequency. However, those analyses in the shadowed region have not been studied yet.

This paper aims to derive an additional term between creeping diffraction from a dielectric circular cylinder and edge diffraction from an absorber screen in the shadowed region. In addition, a uniform additional term is proposed to unify the formulations in the lit and shadowed regions.

The additional term proposed in this work is different from the finger field mentioned in the PTD [33]. The PTD improves the accuracy of the physical optics (PO) [34] by introducing the fringe wave derived from the analytic solution based on PO. The fringe wave can be seen as the difference between the PO and GTD diffraction coefficients. However, the additional term proposed in this work is the difference between the edge and creeping diffraction coefficients of the UTD. Therefore, the proposal in this work is different from the finger field in the PTD.

The remainder of this paper is organized as follows. The formulation of an additional term in the shadowed region is derived in Section 2. A uniform additional term in the lit and shadowed regions is proposed in Section 3. The validation of the proposal by using the simulation of the exact solutions of a dielectric circular cylinder is conducted, and the results are shown in Section 4. A discussion of results is explained in Section 5. Finally, Section 6 concludes this work, as well as the limitation of this work and future work.

2. PROPOSED MODEL IN THE SHADOWED REGION

In this section, the proposed model is introduced in (1)–(5) first, and then its derivation will be explained in (6)–(18). For the sake of simplicity, the two-dimensional (2D) problems of the infinite-height objects with incident plane waves are considered.

As shown in Fig. 1, an additional term A^{c} between creeping diffraction and edge diffraction in the shadowed region is proposed as

$$E^{\mathrm{c}} \approx E^{\mathrm{d}} + A^{\mathrm{c}}, \tag{1}$$

$$A^{\mathrm{c}} = -E^{\mathrm{i}} M \sqrt{\frac{2}{k_0}} p^*(\xi^{\mathrm{c}}, q_{\mathrm{s,h}}) e^{-\mathrm{j}k_0 a\theta} e^{-\mathrm{j}\frac{\pi}{4}} \frac{e^{-\mathrm{j}k_0 s}}{\sqrt{s}} \tag{2}$$

with

$$\xi^{\mathrm{c}} = M\theta, \tag{3}$$

$$q_{\mathrm{s,h}} = -\mathrm{j}M \left(\frac{\eta_0}{\eta_{\mathrm{d}}}\right)^{\pm 1}, \tag{4}$$

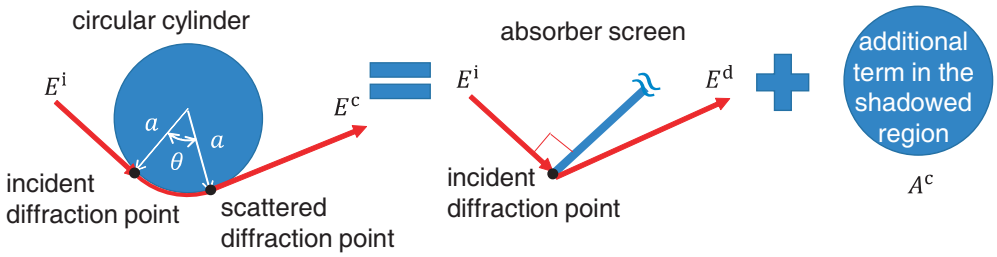

Figure 1. Model of the proposal in the shadowed region.

$$M = \left(\frac{k_0 a}{2}\right)^{\frac{1}{3}} \tag{5}$$

where E^{c} denotes the creeping diffracted electric field from a dielectric circular cylinder. The quantity E^{i} denotes the incident wave to the object, whose direction can be arbitrary. The quantity E^{d} denotes the edge diffracted electric field from an absorber screen, which is generalized from the incident diffraction point with a direction perpendicular to the incident direction. Parameter a denotes the radius of the circular cylinder. Parameter s denotes the distance from the diffraction point to the receiver (Rx). Parameter θ denotes the center angle of the circle. Quantities M and ξ^{c} are the UTD parameters mentioned in [3–5]. Quantities q_{s} and q_{h} are parameters related to the boundary condition for the perpendicular polarization (soft) and parallel polarization (hard), respectively. The $\pm$ sign in (4) is directly associated with the s, h subscript of q. Quantity k_0 denotes the wave number in the free space. Quantities η_0 and η_{d} denote the free-space impedance and surface impedance of the dielectric cylinder, respectively. Function $p^*(\cdot)$ denotes the associated Fock-type integral, which is explained in Appendix A.

Similar to the work in [32], which only studies in the lit region, the application of (1) is that we can separate the contribution of the shadowed FZ and boundary conditions (i.e., the surface impedance and polarization) in the entire lit and shadowed regions. Since edge diffraction E^{d} is determined by the shadowed FZ alone while the key factor $q_{\mathrm{s,h}}$ corresponding to the boundary conditions (i.e., surface impedance and polarization) is directly associated with the additional term A^{c}, the contribution of the shadowed FZ and boundary conditions can be separated by (1).

A detailed derivation of the proposed formula is explained as follows. As shown in Fig. 2(a), the diffracted field from an absorber screen derived from [1, 2] can be calculated as

$$E^{\mathrm{d}} = E^{\mathrm{i}} D \frac{e^{-\mathrm{j}k_0 s^{\mathrm{d}}}}{\sqrt{s^{\mathrm{d}}}} \tag{6}$$

with

$$D = \frac{-e^{-\mathrm{j}\frac{\pi}{4}}}{2\sqrt{2\pi k_0}} \sec\frac{\phi^{\mathrm{d}} - \phi^{\mathrm{i}}}{2} F\left(2k_0 s^{\mathrm{d}} \cos^2\frac{\phi^{\mathrm{d}} - \phi^{\mathrm{i}}}{2}\right) \tag{7}$$

where D denotes the edge diffraction coefficient of an absorber screen. Parameter s^{d} denotes the distance from the diffraction point to the Rx in Fig. 2(a). Parameters ϕ^{i} and ϕ^{d} denote the angles of the incident

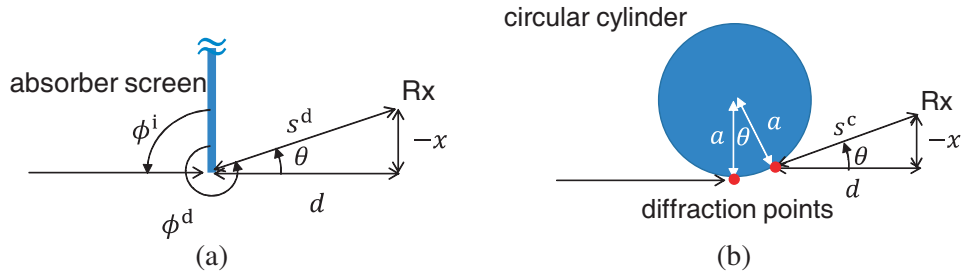

Figure 2. Parameters of the models. (a) Model of edge diffraction. (b) Model of creeping diffraction.

and diffracted rays, respectively, measured in a plane perpendicular to the edge at the diffraction point. Function $F(\cdot)$ is the modified Fresnel integral mentioned in [1]. Parameter d is the distance parallel to the direction of an incident wave from the diffraction point to the Rx. Parameters x and $-x$ are the distances perpendicular to the direction of the incident wave from the diffraction point to the Rx in the lit and shadowed regions, respectively.

For $x < 0$, the small argument of the edge diffraction coefficient derived in [1] is approximated as

$$D \approx \frac{\sqrt{2\pi k_0 s^{\mathrm{d}}} + 2k_0 s^{\mathrm{d}} \left(\pi - \left(\phi^{\mathrm{d}} - \phi^{\mathrm{i}}\right)\right) e^{\mathrm{j}\frac{\pi}{4}}}{2\sqrt{2\pi k_0}}. \tag{8}$$

Since the diffraction points in Figs. 2(a)–2(b) can be seen as one point for $x \to 0$, the slope angle of the direction of diffraction in Figs. 2(a)–2(b) is equal to the center angle θ in Fig. 2(b). Therefore, $\phi^{\mathrm{d}} - \phi^{\mathrm{i}}$ can be approximated as $\pi + \theta$. By applying the small argument of the sine function, we have

$$\pi - \left(\phi^{\mathrm{d}} - \phi^{\mathrm{i}}\right) \approx \pi - (\pi + \theta) = -\theta \approx -\sin\theta = \frac{x}{s^{\mathrm{d}}}. \tag{9}$$

By substituting (8) and (9) into (6), edge diffraction can be asymptotically approximated as

$$E^{\mathrm{d}} \approx \frac{1}{2} E^{\mathrm{i}} e^{-\mathrm{j}k_0 s^{\mathrm{d}}} + E^{\mathrm{i}} \frac{e^{-\mathrm{j}k_0 s^{\mathrm{d}}} e^{\mathrm{j}\frac{\pi}{4}}}{\sqrt{2\pi s^{\mathrm{d}}}} \sqrt{k_0} x = \frac{1}{2} E^{\mathrm{i}} e^{-\mathrm{j}k_0 s^{\mathrm{d}}} - E^{\mathrm{i}} \frac{e^{-\mathrm{j}k_0 s^{\mathrm{d}}} e^{\mathrm{j}\frac{\pi}{4}}}{\sqrt{2\pi s^{\mathrm{d}}}} \sqrt{k_0} |x| \tag{10}$$

given that the condition $|k_0 x| < 1$ rad is held according to the radius of convergence for the Taylor series expansion.

On the other hand, creeping diffraction from a dielectric circular cylinder derived from [3–5] is calculated as

$$E^{\mathrm{c}} = E^{\mathrm{i}} C \frac{e^{-\mathrm{j}k_0 s^{\mathrm{c}}}}{\sqrt{s^{\mathrm{c}}}} \tag{11}$$

with

$$C = -M e^{-\mathrm{j}k_0 a\theta} \sqrt{\frac{2}{k_0}} \left\{ \frac{e^{-\mathrm{j}\frac{\pi}{4}}}{2\sqrt{\pi}\xi^{\mathrm{c}}} \left[1 - F(X)\right] + \hat{P}\left(\xi^{\mathrm{c}}, q_{\mathrm{s,h}}\right) \right\}, \tag{12}$$

$$X = \frac{k_0 s^{\mathrm{c}} \xi^{\mathrm{c}2}}{2M^2} \tag{13}$$

where C denotes the creeping diffraction coefficient. The quantity X is the UTD parameter mentioned in [3–5]. Parameter s^{c} denotes the distance from the diffraction point to the Rx in Fig. 2(b). Function $\hat{P}(\cdot)$ denotes the Fock-type integral, which is explained in Appendix A.

For $x \to 0$, (3) and (13) can be approximated as

$$\xi^{\mathrm{c}} \approx M \sin\theta = -M \frac{x}{s^{\mathrm{c}}}, \quad X \approx \frac{k_0 x^2}{2s^{\mathrm{c}}} \tag{14}$$

given that $\theta < 5^\circ$ is satisfied according to the condition of the approximation $\sin\theta \approx \theta$. The vertical component of s^{c} is also considered as x because of $s^{\mathrm{d}} \approx s^{\mathrm{c}}$ for $x \to 0$. The associated Fock-type integral in (15) and the small argument of the Fresnel integral in (16) are applied as

$$\hat{P}(\xi^{\mathrm{c}}, q_{\mathrm{s,h}}) = \left(p^*(\xi^{\mathrm{c}}, q_{\mathrm{s,h}}) - \frac{1}{2\sqrt{\pi}\xi^{\mathrm{c}}} \right) e^{-\mathrm{j}\frac{\pi}{4}}, \tag{15}$$

$$F(X) \approx \left(\sqrt{\pi X} - 2X e^{\mathrm{j}\frac{\pi}{4}} \right) e^{\mathrm{j}\left(\frac{\pi}{4} + X\right)}. \tag{16}$$

By substituting (14)–(16) into (11), creeping diffraction can be asymptotically approximated as

$$E^{\mathrm{c}} \approx \frac{1}{2} E^{\mathrm{i}} e^{-\mathrm{j}k_0 s^{\mathrm{c}}} - E^{\mathrm{i}} \frac{e^{-\mathrm{j}k_0 s^{\mathrm{c}}} e^{\mathrm{j}\frac{\pi}{4}}}{\sqrt{2\pi s^{\mathrm{c}}}} \sqrt{k_0} |x| - E^{\mathrm{i}} M \sqrt{\frac{2}{k_0}} p^*\left(\xi^{\mathrm{c}}, q_{\mathrm{s,h}}\right) e^{-\mathrm{j}k_0 a\theta} e^{-\mathrm{j}\frac{\pi}{4}} \frac{e^{-\mathrm{j}k_0 s^{\mathrm{c}}}}{\sqrt{s^{\mathrm{c}}}} \tag{17}$$

given that the condition $|k_0 x| < 1$ rad is held. Parameter s can denote either s^{d} or s^{c} because of $s^{\mathrm{d}} \approx s^{\mathrm{c}}$ for $x \to 0$. Therefore, by comparing (10) and (17), the additional term A^{c} in the shadowed region is proposed as

$$A^{\mathrm{c}} = -E^{\mathrm{i}} M \sqrt{\frac{2}{k_0}} p^*\left(\xi^{\mathrm{c}}, q_{\mathrm{s,h}}\right) e^{-\mathrm{j}k_0 a\theta} e^{-\mathrm{j}\frac{\pi}{4}} \frac{e^{-\mathrm{j}k_0 s}}{\sqrt{s}}. \tag{18}$$

3. UNIFICATION OF FORMULAS IN THE LIT AND SHADOWED REGIONS

In our previous work [32], an additional term A^{r} between the reflected and diffracted fields in the lit region was proposed as

$$E^{\mathrm{r}} \approx E^{\mathrm{d}} + A^{\mathrm{r}}, \tag{19}$$

$$A^{\mathrm{r}} = -E^{\mathrm{i}} M \sqrt{\frac{2}{k_0}} p^*\left(\xi^{\mathrm{r}}, q_{\mathrm{s,h}}\right) e^{-\mathrm{j}\frac{\xi^{\mathrm{r}3}}{12}} e^{-\mathrm{j}\frac{\pi}{4}} \frac{e^{-\mathrm{j}k_0 s}}{\sqrt{s}} \tag{20}$$

with

$$\xi^{\mathrm{r}} = -2M\cos\theta^{\mathrm{i}} \tag{21}$$

where E^{r} denotes the reflected electric field from a dielectric circular cylinder. Parameter θ^{i} denotes the incident angle, as shown in Fig. 3. Quantity ξ^{r} is the UTD parameter mentioned in [3–5].

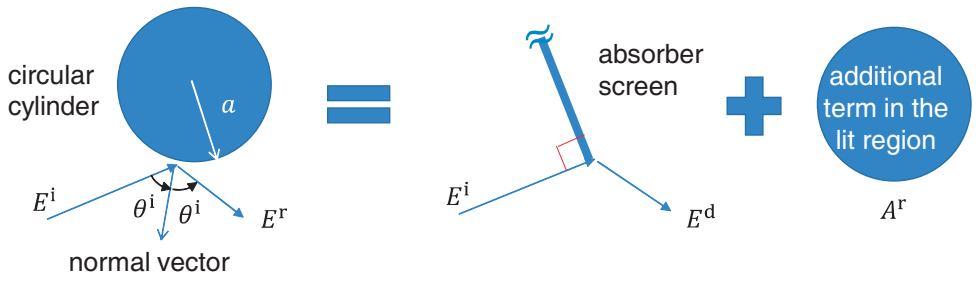

Figure 3. Model of the proposal in the lit region.

In this section, a uniform additional term in the lit and shadowed regions is proposed. The small argument of ξ^{r} is derived in [32] as

$$\xi^{\mathrm{r}} \approx -M\frac{x}{s^{\mathrm{r}}} \tag{22}$$

where s^{r} is the distance from the reflection point to Rx. Because of $s^{\mathrm{c}} \approx s^{\mathrm{r}}$ for $x \to 0$, we have $\xi^{\mathrm{c}} \approx \xi^{\mathrm{r}}$ for $x \to 0$ by comparing (14) with (22). Accordingly, ξ can denote either ξ^{c} or ξ^{r}. In addition, both θ in (2) and $\xi^{\mathrm{r}3}$ in (20) approach zero for $x \to 0$. Therefore, A^{c} in (2) and A^{r} in (20) can be approximately unified to one equation as

$$A^{\mathrm{r}} \approx A^{\mathrm{c}} \approx A^{\mathrm{u}} = -E^{\mathrm{i}} M \sqrt{\frac{2}{k_0}} p^*(\xi, q_{\mathrm{s,h}}) e^{-\mathrm{j}\frac{\pi}{4}} \frac{e^{-\mathrm{j}k_0 s}}{\sqrt{s}} \tag{23}$$

where A^{u} denotes the uniform additional term for both lit and shadowed regions. The cases of $\xi > 0$, $\xi < 0$, and $\xi = 0$ represent that the Rx is in the lit region, shadowed region, and SB, respectively. Although $|k_0 x| < 1$ rad is the condition of the approximations (10) and (17), it is not the condition of the proposal (23). From the validation in the next section, we will find that the proposal is still valid for $|k_0 x| > 400$ rad.

4. VALIDATION OF PROPOSAL

In this section, the simulations using the exact solution of a dielectric circular cylinder are conducted to validate the methods including the proposals. Specifically, the validation is designed to evaluate the effect of the additional terms $A^{\mathrm{c,r,u}}$. Therefore, edge diffraction adding the additional term is compared with the reflection and creeping diffraction in the lit and shadowed regions, respectively.

Figure 4(a) shows the simulation environments of a semi-infinite-long absorber screen to calculate edge diffraction E^{d}. The width of the screen is set to $2a$. Fig. 4(b) shows the simulation environments of a dielectric circular cylinder to calculate creeping diffraction or reflection $E^{\mathrm{c,r}}$. The radius of the circular cylinder is set to a. A uniform plane wave is incident to the object. The continuous wave (CW) is used for simulation. Parameters x and d are distances perpendicular and parallel to the incident wave

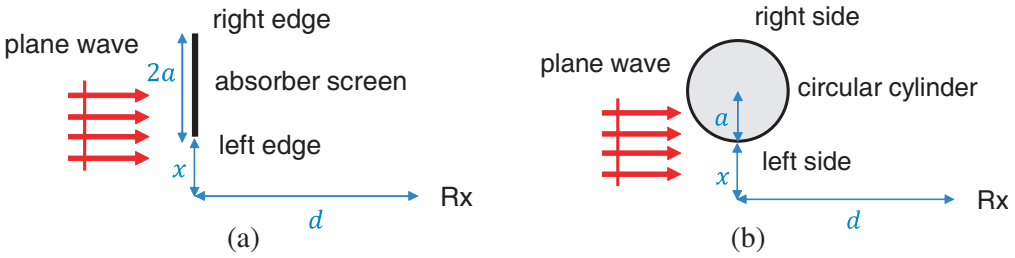

Figure 4. Simulation environment (top view). (a) Model of an absorber screen. (b) Model of a dielectric circular cylinder.

from the object to the Rx, respectively. The cases of $x > 0$ and $x < 0$ represent the lit and shadowed regions, respectively. Parameter f denotes the center frequency, which is considered at the mmWave and sub-THz bands. Parameter $\dot{\epsilon}_{\mathrm{r}}$ denotes the relative complex permittivity of the dielectric circular cylinder. The relative complex permittivity and the dimension of the human skin are used [35]. Each parameter of the simulation is summarized in Table 1.

Table 1. Simulation parameters.

Parameters	Values
f (GHz)	40, 60, 80, 100
x (m)	$[-0.2, 0.2]$
d (m)	2
a (m)	0.2
$\dot{\epsilon}_{\mathrm{r}}$	$11.7 - \mathrm{j}14.3$ (at 40 GHz) $8.0 - \mathrm{j}10.9$ (at 60 GHz) $6.4 - \mathrm{j}8.6$ (at 80 GHz) $5.6 - \mathrm{j}7.1$ (at 100 GHz)
E^{i} (V/m)	1

There are four methods in the simulation, i.e., the UTD, proposal ($A^{\mathrm{r,c}}$), proposal (A^{u}), and exact solution. As a reference of accuracy, the exact solution calculates the total field using the eigen-function expansions as shown in Appendix B. In the UTD, the total field E^{UTD} is calculated as

$$E^{\mathrm{UTD}} = \begin{cases} E^{\mathrm{i}} e^{-\mathrm{j}k_0 d} + E^{\mathrm{c}}_{\mathrm{r}} + E^{\mathrm{r}}_{\mathrm{l}} & \text{(lit region)} \\ E^{\mathrm{c}}_{\mathrm{r}} + E^{\mathrm{c}}_{\mathrm{l}} & \text{(shadowed region)} \end{cases} \tag{24}$$

where $E^{\mathrm{i}} e^{-\mathrm{j}k_0 d}$ denotes the incident wave to the Rx. The l and r subscripts of E are directly associated with the fields from the left and right of the object, respectively, as shown in Figs. 4(a)–4(b).

In the proposal ($A^{\mathrm{r,c}}$), the total field E^{Pro1} is calculated as

$$E^{\mathrm{Pro1}} = \begin{cases} E^{\mathrm{i}} e^{-\mathrm{j}k_0 d} + E^{\mathrm{d}}_{\mathrm{r}} + E^{\mathrm{d}}_{\mathrm{l}} + A^{\mathrm{c}}_{\mathrm{r}} + A^{\mathrm{r}}_{\mathrm{l}} & \text{(lit region)} \\ E^{\mathrm{d}}_{\mathrm{r}} + E^{\mathrm{d}}_{\mathrm{l}} + A^{\mathrm{c}}_{\mathrm{r}} + A^{\mathrm{c}}_{\mathrm{l}} & \text{(shadowed region)} \end{cases} \tag{25}$$

where l and r subscripts of A are directly associated with the fields from the left and right of the object, respectively, as shown in Figs. 4(a)–4(b).

In the proposal (A^{u}), the total field E^{Pro2} is calculated as

$$E^{\mathrm{Pro2}} = \begin{cases} E^{\mathrm{i}} e^{-\mathrm{j}k_0 d} + E^{\mathrm{d}}_{\mathrm{r}} + E^{\mathrm{d}}_{\mathrm{l}} + A^{\mathrm{u}}_{\mathrm{r}} + A^{\mathrm{u}}_{\mathrm{l}} & \text{(lit region)} \\ E^{\mathrm{d}}_{\mathrm{r}} + E^{\mathrm{d}}_{\mathrm{l}} + A^{\mathrm{u}}_{\mathrm{r}} + A^{\mathrm{u}}_{\mathrm{l}} & \text{(shadowed region)} \end{cases} \tag{26}$$

The processor of the calculating computer is an Intel(R) Core(TM) i9-12900K CPU @ 3.19 GHz. The usable installed memory of the calculating computer is 63.7 GB. The system type of the calculating computer is a 64-bit operating system with an ×64-based processor. The simulation software is MATLAB.

Figures 5–8 show the plots of the spatial distributions of the normalized receiving power (NRP), which is the power density of the total field normalized by a free-space incident wave, at 40, 60, 80, and 100 GHz, respectively. For each frequency, both perpendicular polarization (perp.) and parallel polarization (para.) are simulated. Parameter x is varied from -0.2 to 0.2 m with an interval of 0.02 m, and hence each figure has 200 tests. The results show that the proposal (A^{u}) and UTD are in good agreements with the exact solution. Considering the exact solution as a reference, the authors calculate

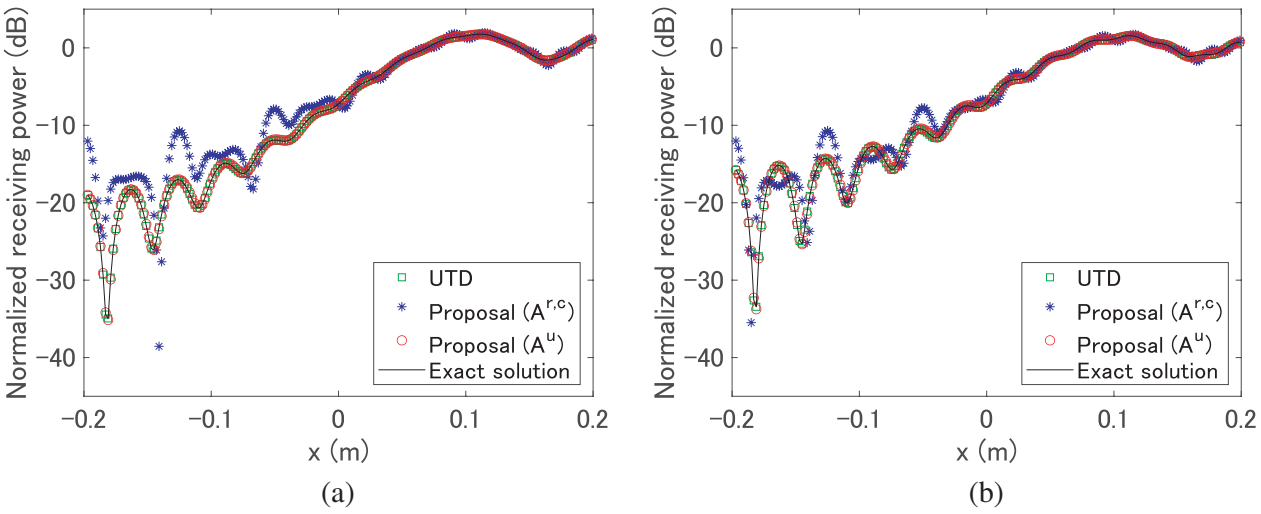

Figure 5. Validation of the proposed model at 40 GHz. (a) Perpendicular polarization. (b) Parallel polarization.

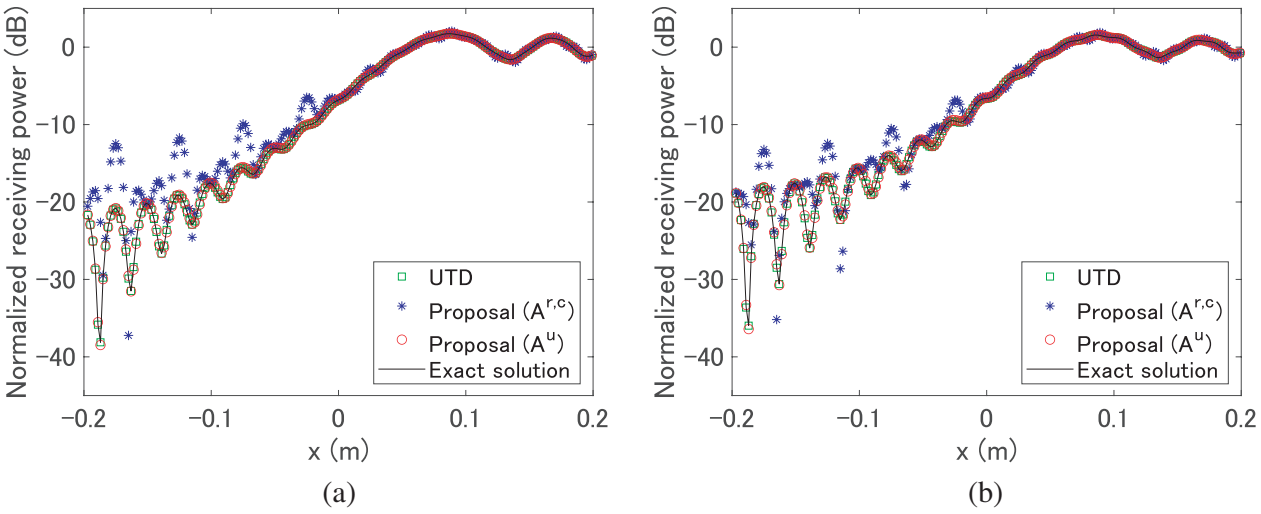

Figure 6. Validation of the proposed model at 60 GHz. (a) Perpendicular polarization. (b) Parallel polarization.

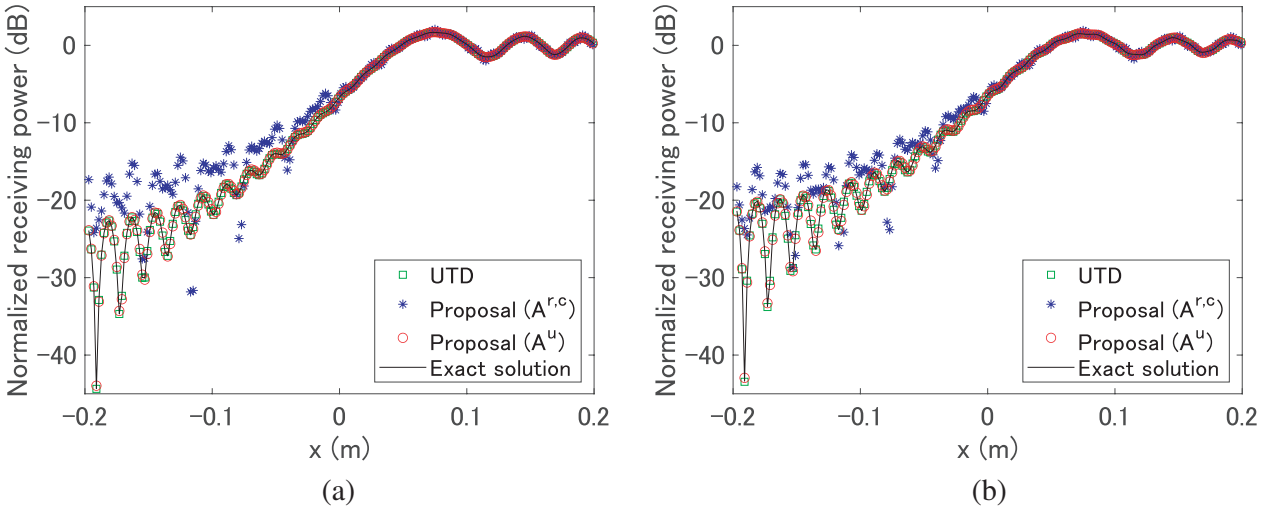

Figure 7. Validation of the proposed model at 80 GHz. (a) Perpendicular polarization. (b) Parallel polarization.

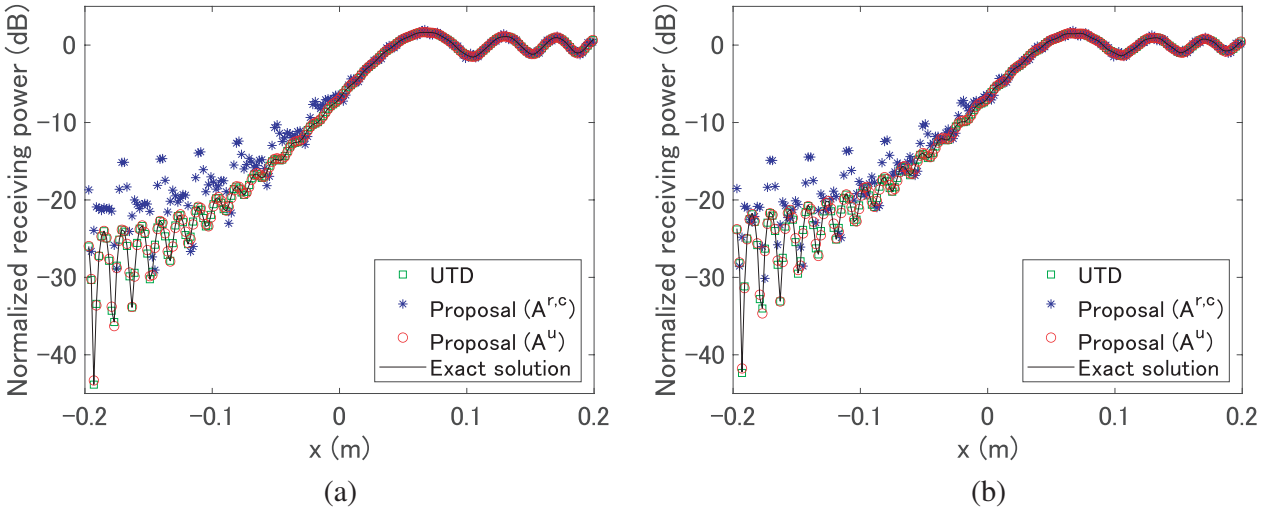

Figure 8. Validation of the proposed model at 100 GHz. (a) Perpendicular polarization. (b) Parallel polarization.

the root-mean-square error (RMSE) by (27).

$$\mathrm{RMSE} = \sqrt{\sum_{i=1}^{m} \frac{\left(\mathrm{NRP}_i^{\mathrm{Method}} - \mathrm{NRP}_i^{\mathrm{Exact}}\right)^2}{m}} \tag{27}$$

where $\mathrm{NRP}_i^{\mathrm{Exact}}$ is the NRP calculated by the exact solution on a dB scale for the ith test. The quantity $\mathrm{NRP}_i^{\mathrm{Method}}$ is the NRP calculated by the other methods on a dB scale for the ith test. Parameter m is the total number of tests per figure (i.e., $m = 200$). The comparison of the RMSEs among all the methods is shown in Table 2.

The results show that the proposal ($A^{\mathrm{r,c}}$) has accuracy with an RMSE of over 1 dB. However, the proposal (A^{u}) achieves a good accuracy with a low RMSE of less than 0.2 dB as well as the UTD, compared with the exact solution. Therefore, the uniform additional term is validated in the lit and shadowed regions. More validation results are shown in Appendix B. The comparison of the average computational time for each method and frequency is summarized in Table 3.

Table 2. The comparison of the RMSE among the UTD, proposal ($A^{r,c}$), and proposal (A^{u}).

Methods	UTD	Proposal ($A^{r,c}$)	Proposal (A^{u})
40 GHz (perp.)	0.01 dB	3.18 dB	0.09 dB
40 GHz (para.)	0.03 dB	2.00 dB	0.12 dB
60 GHz (perp.)	0.01 dB	3.26 dB	0.11 dB
60 GHz (para.)	0.04 dB	2.37 dB	0.15 dB
80 GHz (perp.)	0.01 dB	3.67 dB	0.14 dB
80 GHz (para.)	0.04 dB	3.50 dB	0.17 dB
100 GHz (perp.)	0.01 dB	3.69 dB	0.16 dB
100 GHz (para.)	0.05 dB	2.95 dB	0.20 dB

Table 3. The comparison of the average computational time for each method and frequency.

Methods	Exact solution	UTD	Proposal (A^{u} or $A^{r,c}$)
40 GHz	0.0141 s	0.0244 s	0.0247 s
60 GHz	0.0182 s	0.0235 s	0.0235 s
80 GHz	0.0231 s	0.0240 s	0.0274 s
100 GHz	0.0351 s	0.0305 s	0.0284 s

From Table 3, we can find that the computational time of the exact solution becomes high when frequency increases. However, similar to UTD, the computational time of the proposal is frequency-independent, since they are analytic approaches.

5. DISCUSSION

From the results shown in Figs. 5–8, we can find that A^{u} and A^{r} work well while A^{c} has an error in the shadowed region. The reason for the error is considered fictitious interference by the phase difference between edge diffraction and additional term. To validate the above consideration, the fields only from the left side of the object are simulated. Simulations in this Section are of the same conditions as Section 4, but simulation methods are different. Four methods are used, i.e., the proposal ($A^{r,c}$), proposal (A^{u}), UTD, and UTD (without A). The UTD is considered a reference to validate the proposal ($A^{r,c}$) and proposal (A^{u}). The UTD (without A) means that reflection or creeping diffraction is replaced by edge diffraction to figure out the role of the additional term. The total field ignoring the field from the right side of the object is defined as the 'left field' E_2. The left fields E_{l}^{Pro1}, E_{l}^{Pro2}, E_{l}^{UTD1}, and E_{l}^{UTD2} for the proposal ($A^{r,c}$), proposal (A^{u}), UTD, and UTD (without A), respectively, are calculated as

$$E_{l}^{Pro1} = \begin{cases} E^{i}e^{-jk_0 d} + E_{l}^{d} + A_{l}^{r} & \text{(lit region)} \\ E_{l}^{d} + A_{l}^{c} & \text{(shadowed region)} \end{cases} \tag{28}$$

$$E_{l}^{Pro2} = \begin{cases} E^{i}e^{-jk_0 d} + E_{l}^{d} + A_{l}^{u} & \text{(lit region)} \\ E_{l}^{d} + A_{l}^{u} & \text{(shadowed region)} \end{cases} \tag{29}$$

$$E_{l}^{UTD1} = \begin{cases} E^{i}e^{-jk_0 d} + E_{l}^{r} & \text{(lit region)} \\ E_{l}^{c} & \text{(shadowed region)} \end{cases} \tag{30}$$

$$E_{l}^{UTD2} = \begin{cases} E^{i}e^{-jk_0 d} + E_{l}^{d} & \text{(lit region)} \\ E_{l}^{d} & \text{(shadowed region)} \end{cases} \tag{31}$$

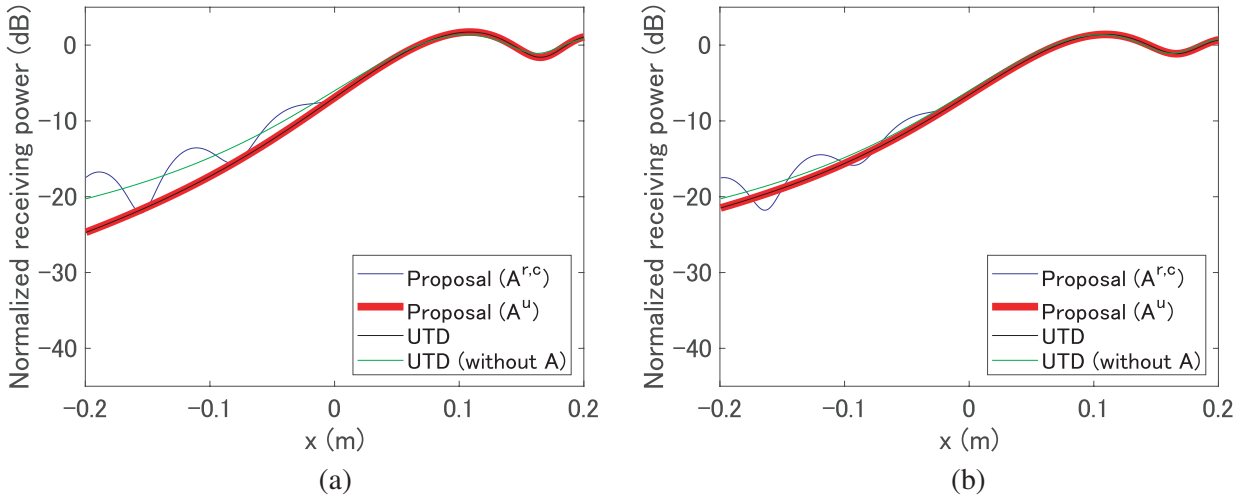

Figure 9. The receiving power of the left field at 40 GHz. (a) Perpendicular polarization. (b) Parallel polarization.

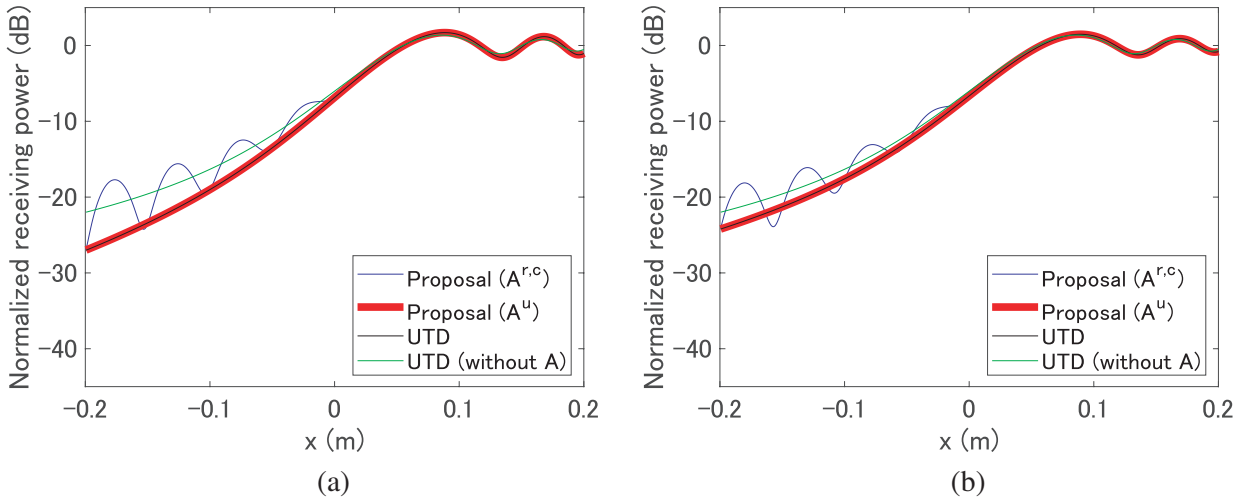

Figure 10. The receiving power of the left field at 60 GHz. (a) Perpendicular polarization. (b) Parallel polarization.

Figures 9–12 show the plots of the NRP of the left field at 40, 60, 80, and 100 GHz, respectively. For each frequency, both perpendicular polarization and parallel polarization are simulated. Parameter x is varied from -0.2 to 0.2 m. To reproduce the ripple of the blue line in Figs. 9–12, each method is simulated 1000 points per figure for the sufficient samples [22]. The results show that the proposal (A^{u}) is in good agreement with the UTD while the proposal ($A^{\mathrm{r,c}}$) has a fictitious interference ripple in the shadowed region. To explain the reason, the phase of each field is analyzed in the shadowed region. According to (11), (6), (18), and (23), the phases of $E_{\mathrm{l}}^{\mathrm{c}}$, $E_{\mathrm{l}}^{\mathrm{d}}$, $A_{\mathrm{l}}^{\mathrm{c}}$, and $A_{\mathrm{l}}^{\mathrm{u}}$ are

$$\arg(E_{\mathrm{l}}^{\mathrm{c}}) \sim k_0 s_{\mathrm{l}} + \frac{\pi}{4}, \tag{32}$$

$$\arg(E_{\mathrm{l}}^{\mathrm{d}}) \sim k_0 s_{\mathrm{l}} + \frac{\pi}{4}, \tag{33}$$

$$\arg(A_{\mathrm{l}}^{\mathrm{c}}) \sim k_0 s_{\mathrm{l}} + \frac{\pi}{4} + k_0 a\theta, \tag{34}$$

$$\arg(A_{\mathrm{l}}^{\mathrm{u}}) \sim k_0 s_{\mathrm{l}} + \frac{\pi}{4} \tag{35}$$

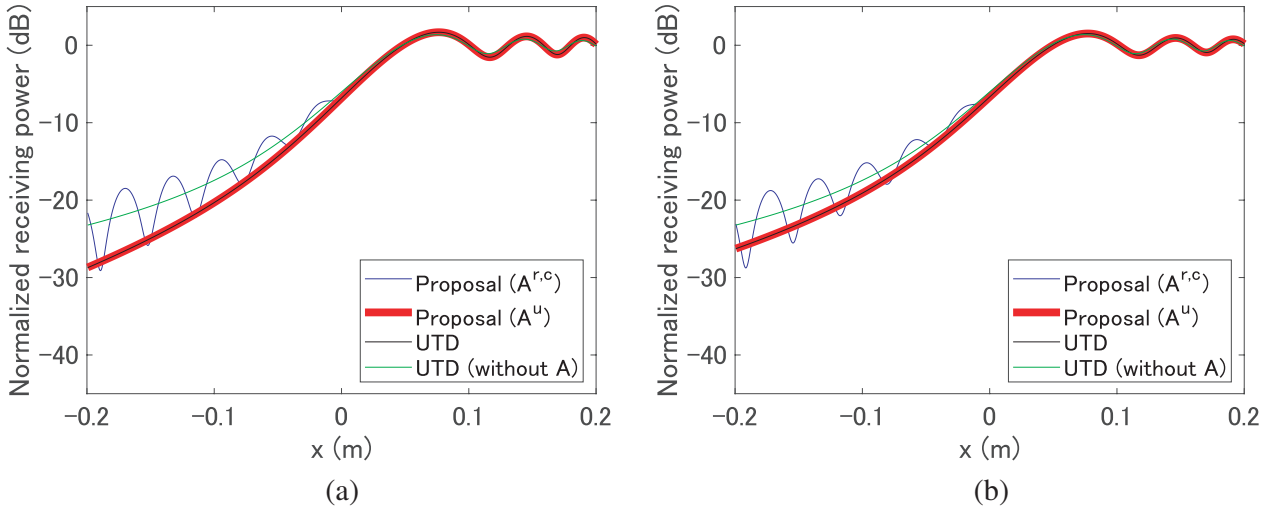

Figure 11. The receiving power of the left field at 80 GHz. (a) Perpendicular polarization. (b) Parallel polarization.

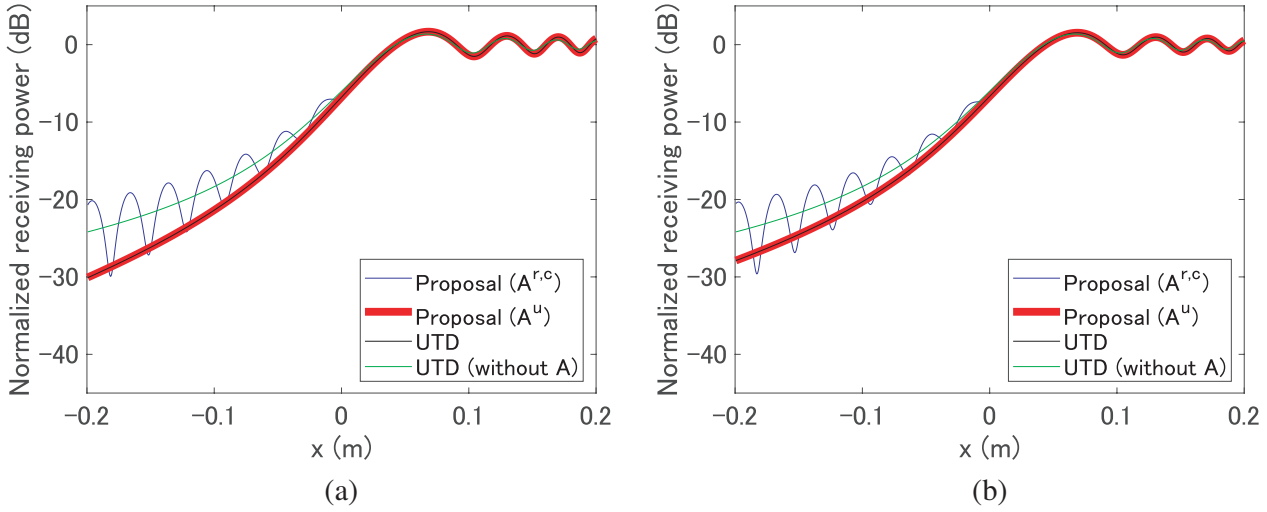

Figure 12. The receiving power of the left field at 100 GHz. (a) Perpendicular polarization. (b) Parallel polarization.

where $\arg(\cdot)$ denotes the phase function. Parameter s_1 is the distance from the left diffraction point to the Rx.

From the phase analysis in (32)–(35), we can figure out the reason for the fictitious interference. For the proposal (A^{u}) in (29), each term in the case of the shadowed region has the same phase, and hence no fictitious interference occurs. However, for the proposal ($A^{\mathrm{r,c}}$) in (28), A_1^{c} and E_1^{d} have different phases, and hence a fictitious interference occurs. Especially, at a high frequency where k_0 is large, the fictitious interference is significant, as shown in Figs. 9–12. That fictitious interference is not significant in the lit region, since the incident wave $E^{\mathrm{i}}e^{-\mathrm{j}k_0 d}$ only exists in the lit region and is dominant (corresponding to 0 dB in Figs. 9–12. Therefore, the contributions of the proposed uniform additional term are not only to unify the formulations in the lit and shadowed regions but also to eliminate the fictitious interference.

Furthermore, Figs. 9–12 show that there is a maximum 5.91 dB gap between the UTDs with and without A. Therefore, the proposed uniform additional term plays a nonnegligible role in accuracy. One application of the proposal is to figure out the structure of the field. Similar to the previous work in [32], the contributions of the shadowed FZ and boundary conditions (i.e., the surface impedance and

polarization) can be separated as

$$E^{\mathrm{r,c}} \approx E^{\mathrm{d}} + A^{\mathrm{u}} \tag{36}$$

where $E^{\mathrm{r,c}}$ denotes either the reflected electric field or the creeping diffracted electric field. Quantities E^{d} and A^{u} correspond to the influences of the shadowed FZ and boundary conditions, respectively.

Through (36), we can analyze the frequency characteristics of the separated terms representing the surface impedance and polarization in the first FZ, where the prediction of the shadowing effect is important in the B5G [32]. Simulation conditions are the same as in Section 4 but use a conducting circular cylinder at 10–100 GHz. Figs. 13(a)–13(b) show the frequency characteristics among the sum of the edge diffracted and incident waves, the sum of the reflected and incident waves, and uniform additional term at the frequencies from 10 to 100 GHz when x is set to 0.03 m (within the first FZ at 100 GHz) in the lit region. Figs. 14(a)–14(b) show the frequency characteristics among edge diffraction, creeping diffraction, and uniform additional term at the frequencies from 10 to 100 GHz when x is set to -0.03 m in the shadowed region. From the results, we can find that the uniform additional term

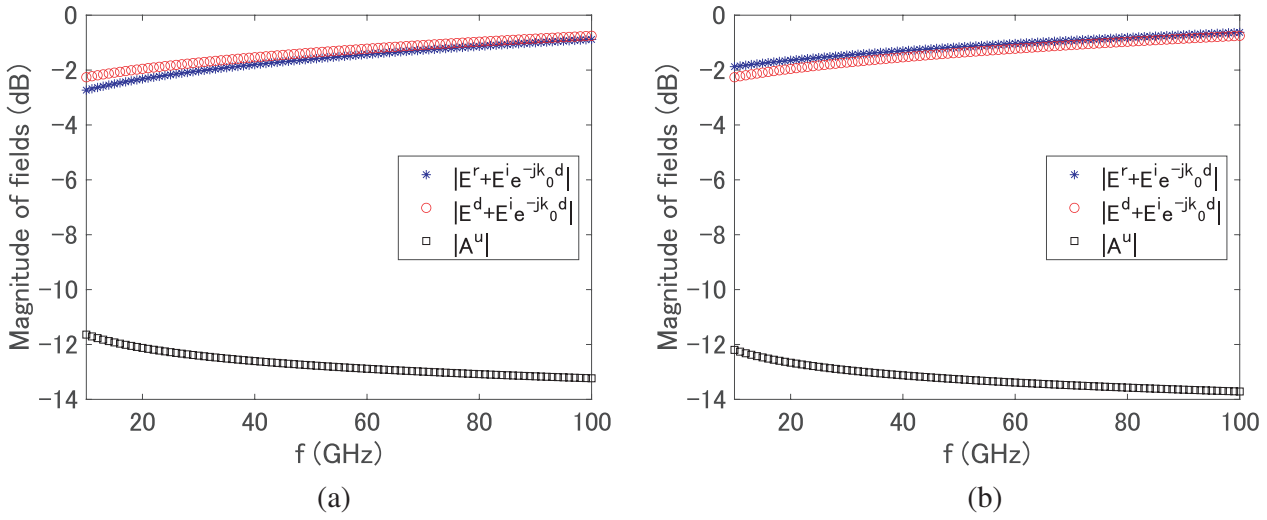

Figure 13. The frequency analysis of the field in the lit region ($x = 0.03$ m). (a) Perpendicular polarization. (b) Parallel polarization.

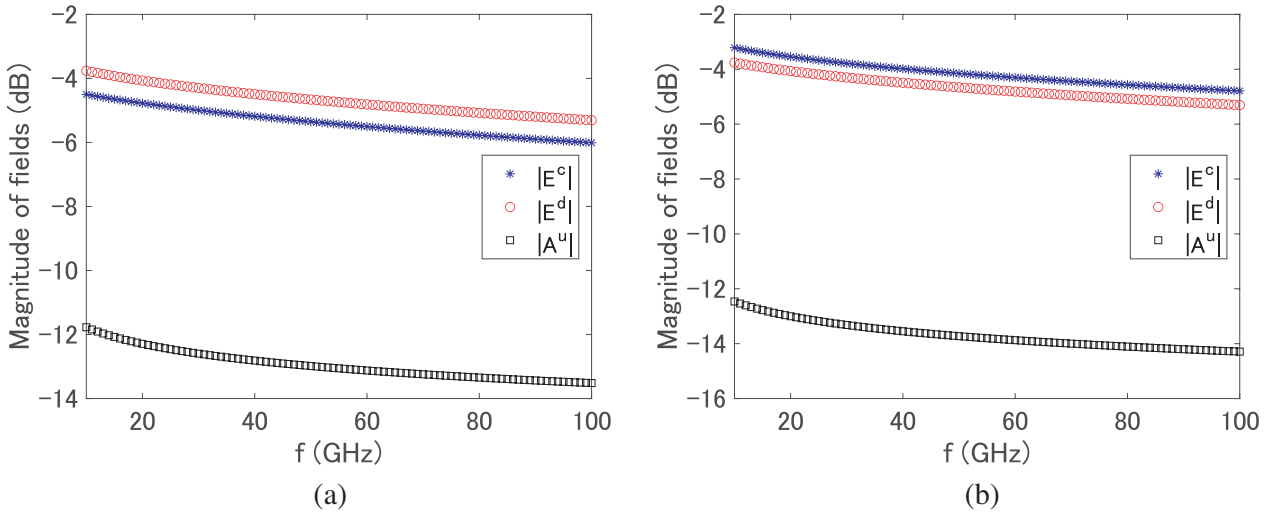

Figure 14. The frequency analysis of the field in the shadowed region ($x = -0.03$ m). (a) Perpendicular polarization. (b) Parallel polarization.

becomes weak when frequency increases, since the magnitude of A^{u} is the order of $f^{-\frac{1}{6}}$ according to (23) as

$$A^{\mathrm{u}} = -E^{\mathrm{i}} \left(\frac{k_0 a}{2}\right)^{\frac{1}{3}} \sqrt{\frac{2}{k_0}} p^*(\xi, q_{\mathrm{s,h}}) e^{-\mathrm{j}\frac{\pi}{4}} \frac{e^{-\mathrm{j}k_0 s}}{\sqrt{s}} \sim O\left(k_0^{-\frac{1}{6}}\right) \sim O\left(f^{-\frac{1}{6}}\right) \tag{37}$$

where $O(\cdot)$ is the symbol of the order. The other components become strong with an increase in frequency in the lit region according to [32] as

$$\lim_{x\to+0} E^{\mathrm{d}} + E^{\mathrm{i}} e^{-\mathrm{j}k_0 d} \approx \frac{1}{2} E^{\mathrm{i}} e^{-\mathrm{j}k_0 d} + E^{\mathrm{i}} \frac{e^{-\mathrm{j}k_0 s} e^{\mathrm{j}\frac{\pi}{4}}}{\sqrt{2\pi s}} \sqrt{k_0}|x| \sim O\left(k_0^{\frac{1}{2}}\right) \sim O\left(f^{\frac{1}{2}}\right) \tag{38}$$

while they are weak in the shadowed region with an increase in frequency according to (10) as

$$\lim_{x\to-0} E^{\mathrm{d}} \approx \frac{1}{2} E^{\mathrm{i}} e^{-\mathrm{j}k_0 d} - E^{\mathrm{i}} \frac{e^{-\mathrm{j}k_0 s} e^{\mathrm{j}\frac{\pi}{4}}}{\sqrt{2\pi s}} \sqrt{k_0}|x| \sim O\left(-k_0^{\frac{1}{2}}\right) \sim O\left(-f^{\frac{1}{2}}\right). \tag{39}$$

Therefore, at a high frequency, the contribution of the boundary condition is not dominant in the lit region, but it is still significant in the shadowed region.

The contribution of boundary condition is evaluated by simulating the dependencies on the surface impedance and polarization. To evaluate the dependencies on the surface impedance, the exact solutions of the NRPs for a dielectric cylinder and a perfect electric conductor (PEC) circular cylinder are simulated and compared. To check the dependencies on polarization, the exact solutions of NRPs for a dielectric cylinder with perpendicular and parallel polarization are simulated and compared. The size and location of the simulated object are mentioned in Section 4. Fig. 15(a) shows the comparison of the exact solutions between the PEC and human skin for the parallel polarization at 40 GHz. By calculating the RMSEs between PEC and human skin in Fig. 15(a), we can find that there are RMSEs of 0.67 dB and 2.72 dB in the lit ($x > 0$) and shadowed ($x < 0$) regions, respectively. Moreover, Fig. 15(b) shows the comparison of the exact solutions between the perpendicular polarization and parallel polarization for the human skin at 40 GHz. By calculating the RMSEs between perpendicular and parallel polarizations in Fig. 15(b), we can find that there are RMSEs of 0.28 dB and 1.99 dB in the lit ($x > 0$) and shadowed ($x < 0$) regions, respectively. The results imply that there is almost no dependency (less than 1 dB) on boundary conditions (i.e., the surface impedance and polarization) in the lit region while there are a few dependencies (more than 1 dB) on boundary conditions in the shadowed region.

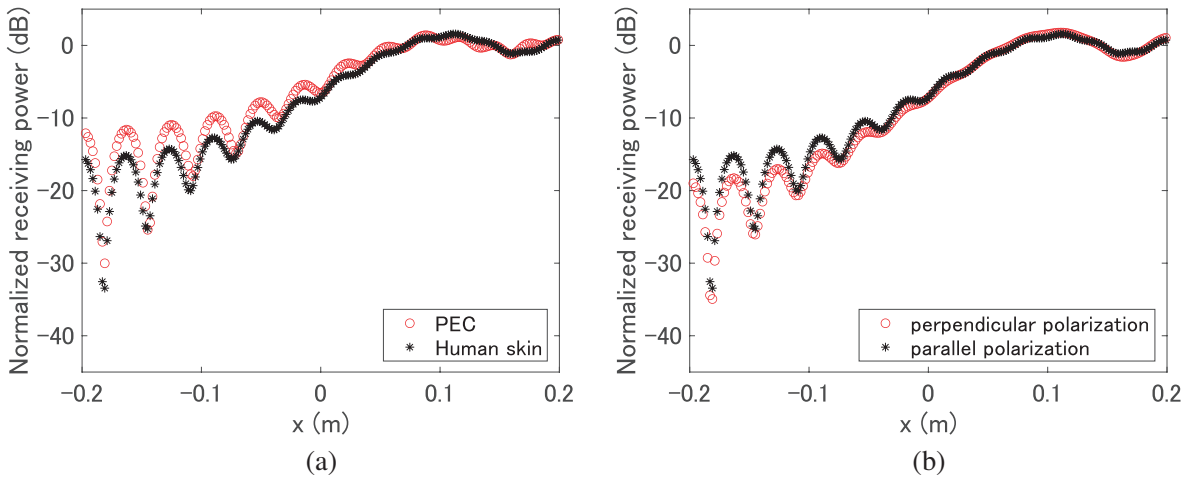

Figure 15. The exact solutions of scattering from a circular cylinder in different boundary conditions. (a) Dependency on the surface impedance. (b) Dependency on polarization.

Although this work only focuses on an absorber screen and a dielectric circular cylinder, it attempts to unify three different propagation mechanisms, i.e., reflection, edge diffraction, and creeping diffraction, by using one formula. The authors expect that people will deeply understand the physical phenomena inside of natural behavior from this work.

6. CONCLUSION

This paper derived an additional term based on a UTD to model the difference between creeping diffraction and edge diffraction from a dielectric circular cylinder and an absorber screen, respectively, in the shadowed region. In addition, a uniform additional term using the Fock-type integral was proposed to unify the formulations in the lit and shadowed regions. The proposals were validated by the UTD and exact solutions of a dielectric circular cylinder at mmWave/sub-THz bands. From the discussion of the results, the proposed uniform additional term could not only unify the formulations in the lit and shadowed regions but also eliminate the fictitious interference. The contributions of the shadowed FZ and boundary conditions (i.e., the surface impedance and polarization) could be separated. The frequency characteristics of the shadowed FZ and boundary conditions were analyzed and simulated near the SB at a high frequency (10 GHz–100 GHz). The results implied that there was almost no dependency (less than 1 dB) on boundary conditions in the lit region while there were a few dependencies (more than 1 dB) on boundary conditions in the shadowed region. Although this work was only limited to a dielectric circular cylinder, it attempted to unify three different propagation mechanisms, i.e., reflection, edge diffraction, and creeping diffraction, by using one formula. In the future, the structure of the field behind an arbitrarily shaped object will be analyzed.

ACKNOWLEDGMENT

This paper was supported by the Commissioned Research through the National Institute of Information and Communications Technology (NICT), Japan, under Grant #02701.

APPENDIX A. COMPUTATION OF THE FOCK-TYPE INTEGRAL

The Fock-type integral $\hat{P}(\cdot)$ is defined as

$$\hat{P}(\xi, q) = \frac{e^{-\mathrm{j}\frac{\pi}{4}}}{\sqrt{\pi}} \int_{-\infty}^{\infty} \frac{v'(\tau) - qv(\tau)}{w_2'(\tau) - qw_2(\tau)} e^{-\mathrm{j}\xi\tau} \mathrm{d}\tau \tag{A1}$$

with

$$v(\tau) = \sqrt{\pi}\mathrm{Ai}(\tau), \tag{A2}$$

$$w_2(\tau) = 2\sqrt{\pi}e^{-\mathrm{j}\frac{\pi}{6}}\mathrm{Ai}\left(e^{-\mathrm{j}\frac{2\pi}{3}}\tau\right) \tag{A3}$$

where $\mathrm{Ai}(\cdot)$ is the Airy integral defined as

$$\mathrm{Ai}(\tau) = \frac{1}{2\pi} \int_{-\infty}^{\infty} e^{\pm\mathrm{j}\left(\frac{t^3}{3}+\tau t\right)} \mathrm{d}t. \tag{A4}$$

Equation (A1) can be calculated by using the associated Fock-type integral as

$$\hat{P}(\xi, q) = \left(p^*(\xi, q) - \frac{1}{2\sqrt{\pi}\xi}\right) e^{-\mathrm{j}\frac{\pi}{4}} \tag{A5}$$

where $p^*(\cdot)$ is the associated Fock-type integral, which can be calculated as

$$p^*(\xi, q) = \frac{1}{2\sqrt{\pi}} \int_0^{\infty} \left\{ \frac{\left[e^{-\mathrm{j}\frac{\pi}{3}}\mathrm{Ai}'(\tau) + q\mathrm{Ai}(\tau)\right] e^{-\mathrm{j}r\xi\tau}}{e^{\mathrm{j}\frac{\pi}{6}}\mathrm{Ai}'\left(e^{\mathrm{j}\frac{2\pi}{3}}\tau\right) + qe^{-\mathrm{j}\frac{\pi}{6}}\mathrm{Ai}\left(e^{\mathrm{j}\frac{2\pi}{3}}\tau\right)} - \frac{\left[\mathrm{Ai}'(\tau) - q\mathrm{Ai}(\tau)\right] e^{-\mathrm{j}\xi\tau}}{e^{\mathrm{j}\frac{\pi}{6}}\mathrm{Ai}'\left(e^{-\mathrm{j}\frac{2\pi}{3}}\tau\right) + qe^{-\mathrm{j}\frac{\pi}{6}}\mathrm{Ai}\left(e^{-\mathrm{j}\frac{2\pi}{3}}\tau\right)} \right\} \mathrm{d}\tau \tag{A6}$$

with

$$r = e^{-\mathrm{j}\frac{2\pi}{3}}. \tag{A7}$$

In MATLAB, $\mathrm{Ai}(\tau)$ and $\mathrm{Ai}'(\tau)$ can be calculated by using the codes of $\mathrm{airy}(\tau)$ and $\mathrm{airy}(1, \tau)$, respectively. The numerical integral in (A6) can be categorized as

$$I(\xi) = \int_0^{\infty} f(\tau) e^{-\mathrm{j}r\xi\tau} \mathrm{d}\tau. \tag{A8}$$

To evaluate the above type of numerical integration, a simple extension of a Fourier quadrature method [5] is applied as

$$I(\xi) \approx f(0)\left(\frac{1}{\mathrm{j}r\xi} - \frac{e^{-\mathrm{j}Tr\xi}}{T(r\xi)^2} + \frac{1}{T(r\xi)^2}\right) + T\frac{\sin^2(Tr\xi/2)}{(Tr\xi/2)^2}\sum_{n=1}^{N} f(\tau_n)e^{-\mathrm{j}nTr\xi} \tag{A9}$$

where T and N are the sampling interval and sampling number set to 0.1 and 180, respectively [5].

APPENDIX B. SCATTERING FROM A CIRCULAR CYLINDER

The electric field of a uniform plane wave is assumed to be incident, as shown in Fig. B1(a). The total electric field $E^{\mathrm{Exact}}(\cdot)$ scattered from a dielectric circular cylinder can be expressed as

$$E^{\mathrm{Exact}}(\rho,\phi) = E^{\mathrm{i}}(\rho,\phi) + E^{\mathrm{i}}\left(\rho,\pm\frac{\pi}{2}\right)\sum_{n=-\infty}^{\infty} \mathrm{j}^{-n} a_n H_n^{(2)}\left(k_0\rho\right) e^{\mathrm{j}n\phi} \tag{B1}$$

with

$$a_n = \frac{-\dot{\epsilon}_{\mathrm{r}}^{\pm\frac{1}{2}} J_n\left(k_0 a\right) J_n'\left(\dot{k}_{\mathrm{d}} a\right) + J_n'\left(k_0 a\right) J_n\left(\dot{k}_{\mathrm{d}} a\right)}{\dot{\epsilon}_{\mathrm{r}}^{\pm\frac{1}{2}} H_n^{(2)}\left(k_0 a\right) J_n'\left(\dot{k}_{\mathrm{d}} a\right) - H_n^{(2)\prime}\left(k_0 a\right) J_n\left(\dot{k}_{\mathrm{d}} a\right)} \tag{B2}$$

where ρ denotes the distance from the center of the circular cylinder to the Rx. Parameter ϕ denotes the azimuth angle of Rx measured from the incident direction, as shown in Fig. A1(a). Quantity $E^{\mathrm{i}}(\rho,\phi)$ denotes the incident electric field at the point (ρ,ϕ). Functions $J_n(\cdot)$ and $H_n^{(2)}(\cdot)$ denote the Bessel function of the first kind and the Hankel function of the second kind, respectively, for the nth order. Functions $J_n'(\cdot)$ and $H_n^{(2)\prime}(\cdot)$ are the derivatives of $J_n(\cdot)$ and $H_n^{(2)}(\cdot)$, respectively. The $\pm$ sign in (B2) is directly associated with perpendicular and parallel polarizations. $\dot{k}_{\mathrm{d}}$ denotes the complex wave number in the dielectric cylinder. Parameters a and $\dot{\epsilon}_{\mathrm{r}}$ denote the radius and relative complex permeability of the circular cylinder, respectively. The real and imaginary parts of $\dot{\epsilon}_{\mathrm{r}}$ correspond to the relative permittivity and conductivity, respectively. Especially for a PEC, where the conductivity is infinity, the coefficient is reduced as

$$a_n^{\mathrm{PEC}} = \begin{cases} -J_n(k_0a)/H_n^{(2)}(k_0a) & \text{(for perpendicular polarization)} \\ -J_n'(k_0a)/H_n^{(2)\prime}(k_0a) & \text{(for parallel polarization)} \end{cases} \tag{B3}$$

where the derivation of coefficients a_n and a_n^{PEC} can be found in Chapter 11 of [15].

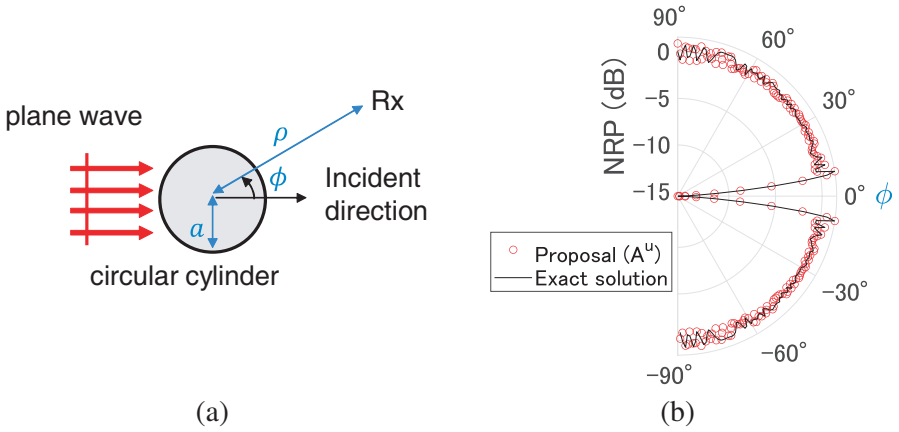

(a) (b)

Figure A1. The scattering from a circular cylinder. (a) Simulation model. (b) Simulation results ($a = 0.2\,\mathrm{m}$, $\rho = 2\,\mathrm{m}$, $f = 40\,\mathrm{GHz}$, $\dot{\epsilon}_{\mathrm{r}} = 11.7 - \mathrm{j}14.3$, and parallel polarization).

Figure A1(b) shows the plot of the amplitude variation of the NRPs with respect to observation angle ϕ. The simulation is under the conditions of $a = 0.2\,\mathrm{m}$, $\rho = 2\,\mathrm{m}$, $f = 40\,\mathrm{GHz}$, $\dot{\epsilon}_\mathrm{r} = 11.7 - \mathrm{j}14.3$, and parallel polarization. The RMSE between the proposal and the exact solution is calculated as 0.45 dB. The results show that the proposed method presents a good accuracy, which has a low RMSE of less than 0.5 dB by comparing it with the exact solution.

REFERENCES

1. Kouyoumjian, R. G. and P. H. Pathak, "A uniform geometrical theory of diffraction for an edge in a perfectly conducting surface," *Proc. IEEE*, Vol. 62, No. 11, 1448–1461, Nov. 1974.
2. Andersen, J. B., "UTD multiple-edge transition zone diffraction," *IEEE Trans. Antennas Propag.*, Vol. 45, No. 7, 1093–1097, Jul. 1997.
3. Pathak, P. H., W. Burnside, and R. Marhefka, "A uniform GTD analysis of the diffraction of electromagnetic waves by a smooth convex surface," *IEEE Trans. Antennas Propag.*, Vol. 26, No. 5, 631–642, Sep. 1980.
4. Pathak, P. H., "An asymptotic analysis of the scattering of plane waves by a smooth convex cylinder," *Radio Science*, Vol. 14, No. 3, 419–435, Jun. 1979.
5. Pearson, L., "A scheme for automatic computation of Fock-type integrals," *IEEE Trans. Antennas Propag.*, Vol. 35, No. 10, 1111–1118, Oct. 1987.
6. Freund, D. E., N. E. Woods, H. Ku, and R. S. Awadallah, "Forward radar propagation over a rough sea surface: A numerical assessment of the Miller-brown approximation using a horizontally polarized 3-GHz line source," *IEEE Trans. Antennas Propag.*, Vol. 54, No. 4, 1292–1304, Apr. 2006.
7. Dockery, G. D., R. S. Awadallah, D. E. Freund, J. Z. Gehman, and M. H. Newkirk, "An overview of recent advances for the TEMPER radar propagation model," *2007 IEEE Radar Conf.*, 896–905, 2007.
8. Glaser, J. I., "Bistatic RCS of complex objects near forward scatter," *IEEE Trans. Aerosp. Electron. Syst.*, Vol. 21, No. 1, 70–78, Jan. 1985.
9. Andrews, J. G., S. Buzzi, W. Choi, S. V. Hanly, A. Lozano, A. C. K. Soong, and J. C. Zhang, "What will 5G be?," *IEEE J. Sel. Areas Commun.*, Vol. 32, No. 6, 1065–1082, Jun. 2014.
10. Rangan, S., T. S. Rappaport, and E. Erkip, "Millimeter-wave cellular wireless networks: Potentials and challenges," *Proc. IEEE*, Vol. 102, No. 3, 366–385, Mar. 2014.
11. Doré, J. B., Y. Corre, S. Bicais, J. Palicot, E. Faussurier, D. Ktenas, and F. Bader, "Above −90 GHz spectrum and single-carrier waveform as enablers for efficient Tbit/s wireless communications," *2018 25th Inter. Conf. Telecom. (ICT)*, 274–278, Saint-Malo, France, 2018.
12. MacCartney, G. R., S. Deng, S. Sun, and T. S. Rappaport, "Millimeter-wave human blockage at 73 GHz with a simple double knife-edge diffraction model and extension for directional antennas," *2016 IEEE 84th Vehi. Tech. Conf. (VTC-Fall)*, 1–6, Montreal, QC, Canada, 2016.
13. Sun, S., T. S. Rappaport, R. W. Heath, A. Nix, and S. Rangan, "MIMO for millimeter-wave wireless communications: Beamforming, spatial multiplexing, or both?," *IEEE Commun. Mag.*, Vol. 52, No. 12, 110–121, Dec. 2014.
14. Sun, S., G. R. MacCartney, M. K. Samimi, and T. S. Rappaport, "Synthesizing omnidirectional antenna patterns, received power and path loss from directional antennas for 5G millimeter-wave communications," *Proc. IEEE Global Commun. Conf. (GLOBECOM)*, 3948–3953, San Diego, CA, USA, Dec. 2015.
15. Balanis, C. A., *Advanced Engineering Electromagnetics*, Wiley, Hoboken, New Jersey, USA, 1989.
16. Clemmow, P. C., "Some extension to the method of integration by steepest descent," *Q. J. Mech., Appl. Math. III*, 241–256, 1950.
17. Osipov, A. V. and Tretyakov, S. A., *Modern Electromagnetic Scattering Theory with Applications*, 274–277, Hoboken, New Jersey, USA: Wiley, 2013.
18. Keller, J. B., "Geometric theory of diffraction," *J. Opt. Soc. Am.*, Vol. 52, No. 2, 116–130, 1962.

19. Du, X., K. Saito, J. Takada, and P. Hanpinitsak, "A novel mirror Kirchhoff approximation method for predicting the shadowing effect by a metal cuboid," *Progress In Electromagnetics Research M*, Vol. 104, No. 18, 199–212, Sep. 2021.
20. Du, X. and J. Takada, "Mirror Kirchhoff approximation for predicting shadowing effect by a PEC convex cylinder," *2021 Appl. Computa. Electromagn. Soci.*, Hamilton, Canada, Aug. 2021.
21. Du, X. and J. Takada, "Low computational cost mirror Kirchhoff approximation for predicting shadowing effect," *IEEE Access*, Vol. 10, 23829–23841, Feb. 2022.
22. Du, X. and J. Takada, "Design of parameters of fast Fourier transform for three-dimensional split step parabolic equations and mirror Kirchhoff approximation," *IEEE Access*, Vol. 11, 44964–44976, May 2023.
23. Basdemir, H. D., "Nonuniform currents flowing on a perfectly conducting cylinder," *2011 XXXth URSI General Assembly and Scientific Symposium*, 1–4, Istanbul, Turkey, 2011.
24. Basdemir, H. D., "Fringe waves on an impedance cylinder," *Optik*, Vol. 124, No. 21, 4999–5002, 2013.
25. Qi, Y., B. Currie, W. Wang, P. Y. Chung, C. Wu, and J. Litva, "Measurement and simulation of radio wave propagation in two indoor environments," *Proc. 6th Inter. Symp. Pers.*, 1171–1174, Toronto, Ontario, Canada, 1995.
26. Jacob, M., S. Priebe, A. Maltsev, A. Lomayev, V. Erceg, and T. Kürner, "A ray tracing based stochastic human blockage model for the IEEE 802.11ad 60 GHz channel model," *Proc. 5th Euro. Conf. Antennas Propag. (EUCAP)*, 3084–3088, Rome, Italy, 2011.
27. Villanese, F., N. E. Evans, and W. G. Scanlon, "Pedestrian-induced fading for indoor channels at 2.45, 5.7 and 62 GHz," *2000 IEEE 52nd Vehi. Tech. Conf. (VTC-Fall)*, 43–48, Boston, MA, USA, 2000.
28. Fakharzadeh, M., J. Ahmadi-Shokouh, B. Biglarbegian, M. R. Nezhad-Ahmadi, and S. Safavi-Naeini, "The effect of the human body on indoor radio wave propagation at 57–64 GHz," *2009 IEEE Antennas Propag. Soc. Inter. Symp.*, 1–4, North Charleston, SC, USA, 2009.
29. Duarte Carvalho de Queiroz, A. and L. C. Trintinália, "An analysis of human body shadowing models for ray-tracing radio channel characterization," *2015 SBMO/IEEE MTT-S Inter. Microwave Optoelectron. Conf. (IMOC)*, 1–5, Porto de Galinhas, Brazil, 2015.
30. Tang, C., "Back scattering from dielectric-coated infinite cylindrical obstacles," *J. Appl. Phys.*, Vol. 28, No. 5, 628–633, 1957.
31. Jacob, M., S. Priebe, T. Kürner, M. Peter, M. Wisotzki, R. Felbecker, and W. Keusgen, "Fundamental analyses of 60 GHz human blockage," *Proc. 7th Euro. Conf. Antennas Propag. (EuCAP)*, 117–121, Gothenburg, Sweden, 2013.
32. Du, X. and J. Takada, "Structure of the field behind a dielectric circular cylinder in the lit side of the transition region," *Progress In Electromagnetics Research M*, Vol. 116, No. 9, 103–118, Apr. 2023.
33. Ufimtsev, P. Y., *Fundamentals of the Physical Theory of Diffraction*, 1–48, Wiley, Hoboken, New Jersey, 2013.
34. Ufimtsev, P. Y., "New insight into the classical Macdonald physical optics approximation," *IEEE Trans. Antennas Propag.*, Vol. 50, No. 3, 11–20, Jun. 2008.
35. Wu, T., T. S. Rappaport, and C. M. Collins, "The human body and millimeter-wave wireless communication systems: interactions and implications," *2015 IEEE Inter. Conf. Communi. (ICC)*, London, UK, 2015.